Volume 1 | Number 1 | Jan 2013 | Pages 1–100

Nanoscale

www.rsc.org/nanoscale

ROYAL SOCIETY OF CHEMISTRY

ROYAL SOCIETY OF CHEMISTRY

www.rsc.org/nanoscale

Synthesis of [111]- and {010}-Faceted Anatase TiO₂ Nanocrystals from Tri-Titanate Nanosheets and Their Photocatalytic and DSSCs Performances†

Changdong Chen,[a] Yasushi Ikeuchi,[a] Linfeng Xu,[a] Galhenage A. Sewvandi,[a] Takafumi Kusunose,[a] Yasuhiro Tanaka,[a] Shunsuke Nakanishi,[a] Puhong Wen,[b] and Qi Feng,[a]*

[a] Department of Advanced Materials Science, Faculty of Engineering, Kagawa University, 2217-20 Hayashi-cho, Takamatsu 761-0396, Japan

[b] Department of Chemistry and Chemical Engineering, Baoji University of Arts and Science, 1 Gaoxin Road, Baoji, Shaanxi 721013, P.R. China

† Electronic supplementary information (ESI) available.

∗ Corresponding author. E-mail: feng@eng.kagawa-u.ac.jp; Fax: +81 (0)87-864-2402; Tel: +81 (0)87-864-2402

Abstract

The [111]- and {010}-faceted anatase nanocrystals with controllable crystal size and morphology were synthesized from the tri-titanate $H_2Ti_3O_7$ nanosheets by hydrothermal reaction. The nanostructures and formation reaction mechanism of obtained TiO_2 nanocrystals were investigated using XRD, FE-SEM, and TEM. Furthermore, the photocatalytic and dye-sensitized solar cell (DSSC) performances of the synthesized anatase nanocrystals were also characterized. Two kinds of reactions occur in the formation process of the anatase nanocrystals. One is in situ topochemical conversion reaction of layered titanate structure to anatase structure, and another is the dissolution-deposition reaction on the particle surface, which splits the formed nanosheet-like particles to small TiO_2 nanocrystals. The surface photocatalytic activity and DSSCs performances of the anatase nanocrystals are dependent on the crystal facet exposing on the particles surface, which increases in an order of non-facet < [111]-facet < {010}-facet. The increasing order corresponds to the increasing order of bandgap and energy level of the lowest valence band of the anatase nanocrystals. Furthermore, the facet of anatase also affects the DSSCs performance, which enhances in the order non-facet < [111]-facet < {010}-facet.

KEYWORDS: TiO_2 nanocrystal, crystal facet, topochemical reaction, photocatalyst, dye-sensitized solar cell.

1. Introduction

Titanium dioxide (TiO$_2$) is an environment-friendly functional materials because of its excellent photocatalytic[1,2] and dye-sensitized solar cells (DSSCs) performances,[3-5] low cost, and nontoxicity.[6] The TiO$_2$ materials can be prepared by two kinds of main chemical processes. One is dry chemical process, such as vacuum arc deposition, metal-organic vacuum deposition, and simple thermal pyrolysis in the gas phase or in the solid phase.[7-9] Another is wet chemical process, such as sol-gel and hydrothermal methods.[10,11] Compared with the dry chemical process, the wet chemical process can control crystal phase, particle size, morphology and surface structure more easily by changing concentration and pH value of the reaction solution, reaction time, temperature, and precursor.[12,13]

Recently, the effects of crystal facet on the photocatalytic and photovoltaic performances have attached much attention. Some excellent experimental results and important theoretical calculation to expound the effects of crystal facet on the photocatalytic and photovoltaic performances have been reported.[14-16] Wen et al. in our group have reported the first study on photocatalytic performance of anatase TiO$_2$ nanocrystals with a specific crystal facet of high energy on the surface, and found that {010}-faceted anatase TiO$_2$ nanocrystals exhibit much higher photocatalytic activity than the normal spherical nanocrystals without specific facet on the surface in 2007.[17] The results stimulate other researchers to study the effect of crystal facet on TiO$_2$ photocatalytic properties. Yang et al. have reported synthesis of high percentage of {001}-faceted TiO$_2$ particles using hydrofluoric acid solution, and their results of first-principle quantum chemical calculation suggest that the {001}-facet of anatase is one of reactive facets for the photocatalytic reactions.[18] Meanwhile, Wu et al. have prepared {010}-faceted and {001}-faceted anatase TiO$_2$ nanocrystals, and found that the {010}-faceted nanocrystals exhibit higher photocatalytic activity than the

3

{001}-faceted nanocrystals and commercial P25 sample in degradation of methyl orange.[19] After that, Han et al. have reported that the {001}-faceted anatase TiO_2 nanosheets exhibit the higher photocatalytic activity than the P25 sample.[20] Moreover, Amano et al. have reported {101}-faceted perfect octahedral anatase crystallites exhibit higher photocatalytic activity than the P25 sample.[21] These results indicate that the crystal facet strongly affects the photocatalytic performance of TiO_2. The facet relates both surface atomic arrangement structure and surface electronic band structure, which affect the photocatalytic activity.[22-26]

The hydrothermal process is an effective method to synthesize TiO_2 nanocrystals with controlled particle size and morphology, where the control of crystal morphology means the control of crystal facet on the crystal surface. The hydrothermal reaction can controls the crystal growth process easily; therefore it is an effective method for the synthesis of TiO_2 with a specific facet on the surface.[27-30] Usually, anatase TiO_2 nanocrystals with a specific facet on the surface are synthesized by hydrothermal treatments of the titanium precursors in solutions containing the hydrofluoric acid and organic compounds as crystal growth directing agents.[18, 20] In such solution reaction process, the TiO_2 particles are formed by dissolution-decomposition mechanism. Therefore, synthesis of small nanocrystals with a specific facet on surface, such as nanocrystals with size below 50 nm, is difficult. We have reported a unique and useful hydrothermal soft chemical process for the synthesis of anatase nanocrystals with a specific facet on the surface from layered titanate nanosheets by topochemical conversion reaction. The {010}-faceted anatase nanocrystals can be obtained by hydrothermal treatment of $H_{1.07}Ti_{1.73}O_4$ layered titanate nanosheets with a lepidocrocite-like structure.[17, 31-34] And [111]-faceted anatase nanocrystals can be obtained by topochemical conversion of $H_2Ti_4O_9$ layered titanate nanosheets to anatase under microwave-assisted hydrothermal conditions.[35] These results suggest

that the anatase nanocrystals with different facet on the surface can be synthesized by using different layered titanate nanosheets as the precursor. Although the syntheses of TiO_2 from layered tri-titanates $Na_2Ti_3O_7$ and $H_2Ti_3O_7$ precursors have been reported, the particle size of TiO_2 products are large.[36, 37] Furthermore, synthesis of TiO_2 from the exfoliated $H_2Ti_3O_7$ nanosheets has not been reported yet.

In the present study, we describe hydrothermal synthesis TiO_2 nanocrystals from the exfoliated $H_2Ti_3O_7$ layered titanate nanosheet precursor. We report the first study on the synthesis of anatase nanocrystals with [111]-facet and {010}-facet on the surface from the exfoliated $H_2Ti_3O_7$ nanosheets, and control of their crystal size and morphology. This success gives us an opportunity to study the effects of crystal facet and size on the bandgap, surface electronic band structure, and photocatalytic activity of TiO_2 nanocrystals. The results reveal that the {010}-faceted anatase nanocrystals exhibit higher photocatalytic activity than [111]-faceted anatase nanocrystals and commercial P25 sample, due to the larger bandgap of {010}-facet. Furthermore, the effect of the crystal facet on the DSSCs performance is studied also.

2. Experimental

2.1 Preparations of $Na_2Ti_3O_7$ and $H_2Ti_3O_7$ samples

The sodium tri-titanate ($Na_2Ti_3O_7$) was prepared by solid state reaction. A mixture of Na_2CO_3 (Wako, 99.5%) and TiO_2 (Wako, anatase form, 98.5%) in a molar ratio of 1.1:3 were mixed by ball-milling for 24 hrs, and then the mixture were heated at 900°C for 12 hrs. The 10 g of obtained $Na_2Ti_3O_7$ samples was acid-treated with a 1M HNO_3 solution (1 L) at 80 °C for 24 hrs under stirring conditions to exchange Na ions with H ions to obtain H^+-form tri-titanate $H_2Ti_3O_7$ samples. The acid treatment was repeated again to complete the ion-exchange reaction. And then the tri-titanate

$H_2Ti_3O_7$ sample was washed with distilled water several times and dried using a freeze dryer.

2.2 Preparation of $H_2Ti_3O_7$ nanosheet colloidal solution and TiO_2 nanocrystals

The 2 g of tri-titanate $H_2Ti_3O_7$ sample was hydrothermally treated in a 12.5% tetramethylammonium hydroxide (TMAOH, Wako) solution (20 mL) at 130 ^{o}C for 24 hrs under stirring conditions to intercalate TMA^+ ions into the interlayer of the tri-titanate $H_2Ti_3O_7$ and to obtain a TMA^+-form tri-titanate $H_2Ti_3O_7$ sample. The obtained TMA^+-form $H_2Ti_3O_7$ was dispersed in 150 mL of distilled water at room temperature by stirring for 48 hrs to exfoliate the TMA^+-form tri-titanate $H_2Ti_3O_7$ sample to its nanosheets. The tri-titanate $H_2Ti_3O_7$ nanosheet colloidal solution was obtained after filtration to remove the unexfoliated particles, and the tri-titanate $H_2Ti_3O_7$ nanosheet solution was named TMA-HTO nanosheet solution.

The TiO_2 nanoparticles were prepared by hydrothermal treatment of the obtained TMA-HTO nanosheet solution after adjusting to a desired pH value with a 6 M HCl solution. The 40 mL of pH adjusted TMA-HTO nanosheet solution was sealed in a Teflon-lined stainless steel vessel with internal volume of 80 mL, and then hydrothermally treated at a desired temperature for 24 hrs. After the hydrothermal treatment, the samples were washed with distilled water several times, and finally dried using a freeze dryer. The obtained TiO_2 sample is named TMA-**A**-**B**, where **A** and **B** are the desired temperature of hydrothermal treatment, and desired pH value of the nanosheet solution, respectively.

2.3 Photocatalytic characterization

The 20 mg of obtained TiO_2 sample was added into a 100 mL of 10 ppm methylene blue (MB) aqueous solution and stirred for 2 hrs to disperse the TiO_2 sample well in

the MB solution and to reach MB adsorption equilibrium on TiO_2 nanocrystals surface under dark conditions without UV-irradiation. And then the suspension was illuminated by a 100 W ultraviolet lamp with 300-400 nm wavelength (UVA, Asahi Spectra, LAX-Cute) at room temperature, and the ultraviolet lamp was located at 20 cm away from the suspension under continuously stirring conditions. At every 20 min interval, 3 mL solution was drawn from the suspension and immediately centrifuged to separate the TiO_2 samples from the solution under 10000 rpm for 10 min. The MB concentration in the solution was determined by using a Shimadzu UV-2450 spectrophotometer. The degradation efficiency of MB solution by the photocatalytic reaction was calculated from the variation of the MB concentration in the solutions before and after UV light irradiation. The P25 nanocrystals sample was purchased from Degussa. The ST20 nanocrystals sample was synthesized by hydrothermal treatment of a commercial anatase nanoparticle sample (ST01, Ishihara Sangyo) with crystal size of 7 nm at 200 ^{o}C for 12 hrs.

2.4 Fabrication and characterization of dye-sensitized solar cells

A TiO_2 nanocrystal paste was prepared by mixing TiO_2 nanocrystal sample (0.5 g), ethanol (2.5 g), α-terpineol (2.0 g), 10 wt% solution of ethyl-cellulose 10 (8-14mPas, 1.4 g) , and 10 wt% solution of ethyl-cellulose 45 (45-65mPas, 1.1 g). The mixture was dispersed by ultrasonication for 30 min, and then ball-milling for 72 hrs. After ball-milling, the ethanol was removed from the mixture using a rotary-evaporator. The TiO_2 photoelectrode was prepared as follows. The fluorine-doped tin oxide (FTO) conducting glass plate was cleaned in distilled water and acetone by ultrasonication for 10 min, orderly. Then the FTO glass plate was dipped in 0.1M titanium tetraisopropoxide (TTIP) solutions for 1 min and washed with distilled water and ethanol, dried at room temperature and calcined at 480 ^{o}C for 1 hr to coat the FTO

7

glass surface with a dense TiO_2 thin film. The prepared TiO_2 paste was coated (10×10 mm) on the TTIP-treated FTO glass plates by screen printing technique and kept in an ethanol box until the TiO_2 film surface smoothly and then dried at 120 ^{o}C for 10 min. This process was repeated to obtain a desired thickness of TiO_2 film. After the TiO_2 paste coating, the TiO_2 film was calcined at 450 ^{o}C for 30 min to obtain a TiO_2 porous electrode. The TiO_2 porous electrodes were dipped in the 0.1M TTIP solution for 1 min, and washed with distilled water and ethanol, dried at room temperature and calcined at 480 ^{o}C for 1 h again. After cooling to 80 ^{o}C, the TiO_2 porous electrodes were soaked in a 3×10^{-4} M N719 dye (di-tetrabutylammonium cisbis(isothiocyanato)bis(2,2'-bipyridyl-4,4' -dicarboxylato)ruthenium(II)) solution for 24 hrs at room temperature, and then washed with a t-butyl alcohol and acetonitrile (v/v=50%:50%) mixed solvent.

The DSSCs were comprised of a dye-adsorbed TiO_2 electrode as an anode, a Pt-coated FTO glass as a cathode, and an electrolyte solution between the anode and the cathode. The electrolyte solution contains 0.1M LiI, 0.01M I_2, 0.6M of 1-butyl-3-n-propylimidazolium iodide (BMII), 0.4M 4-tert-butylpyridine (TBP) and 0.1M guanidine thiocyanate (GT) in acetonitrile and valeronitrile (v/v=85%:15%). The photocurrent−voltage characteristic curves for the DSSCs were measured using a Hokuto-Denko BAS100B electrochemical analyzer under irradiation with simulated sunlight of AM 1.5 (100mW/cm^2), using a sunlight simulator (YSS-E40, Yamashita Denso). A light-passing mask was fixed on the surface of FTO glass of the anode to set the effectively irradiating area on the cell as 0.25 cm^2.

2.5 Physical analysis

The crystal structure of the sample was investigated using a powder X-ray diffractometer (Shimadzu, Model XRD-6100) with Cu Kα (λ=0.15418 nm) radiation.

The size and morphology of the samples were characterized by field emission scanning electron microscopy (FE-SEM) (Hitachi, Model S-900). Transmission electron microscopy (TEM) observation and selected-area electron diffraction (SAED) were performed on a JEOL Model JEM-3010 system at 300 kV. The specific surface area of TiO_2 nanoparticles was calculated from the adsorption data using the Brunauer−Emmett−Teller (BET) method. The thickness of the TiO_2 porous film was measure using surface texture measuring instrument (SURFCOM 480A).

3. Results and discussion

3.1 Preparations of tri-titanate $H_2Ti_3O_7$ nanosheet solution

The sodium tri-titanate ($Na_2Ti_3O_7$) as the precursor was prepared by heating a mixture of Na_2CO_3 and TiO_2 at 900 ^{o}C for 12 hrs. And then a Na^+/H^+ ion-exchange treatment of $Na_2Ti_3O_7$ was carried out to prepare $H_2Ti_3O_7$ sample. XRD patterns of $Na_2Ti_3O_7$ and $H_2Ti_3O_7$ samples were shown in Fig. 1. The $Na_2Ti_3O_7$ sample shows an XRD pattern corresponding to JCPDS File No.31-1329 (monoclinic system, space group P21/m, a=0. 9128, b=0.3803, c=0.8562 nm, β=101.6^{o}), indicating that $Na_2Ti_3O_7$ phase with the layered structure is obtained. The basal spacing of the $Na_2Ti_3O_7$ layered structure is 0.83 nm. After the Na^+/H^+ ion-exchange reaction, the $H_2Ti_3O_7$ sample maintains the essential layered structure but the basal spacing changes to 0.79 nm, and XRD pattern corresponds to JCPDS File No.47-0561 (monoclinic system, space group *C2/m*, a=1.6023, b=0.3749, c=0.9191 nm, β=101.45^{o}).

To exfoliate $H_2Ti_3O_7$ layered structure into its nanosheets, tetramethylammonium ions (TMA$^+$) are intercalated into the $H_2Ti_3O_7$ layered structure by hydrothermal treatment of $H_2Ti_3O_7$ sample in a TMAOH solution at 130 ^{o}C. After the hydrothermal treatment, the TMA$^+$-form $H_2Ti_3O_7$ sample maintains the layered structure, which shows main diffraction peaks of (200), (400), and (600) with *d*-values of 1.79, 0.895,

9

and 0.597 nm, respectively (Fig. 1(c)). The increase of basal spacing from 0.79 nm of $H_2Ti_3O_7$ to 1.79 nm reveals that TMA^+ ions are intercalated into the interlayer space of $H_2Ti_3O_7$ sample. The higher hydrothermal treatment temperature of 130 ^oC is necessary to intercalate TMA^+ ions into the $H_2Ti_3O_7$ structure than those for $H_{1.07}Ti_{1.73}O_4$ with lepidocrocite-like layered structure and $H_2Ti_4O_9$ layered titanates. TMA^+ ions can be intercalated into $H_{1.07}Ti_{1.73}O_4$ layered titanate at room temperature,[33] and into $H_2Ti_4O_9$ layered titanate at 90 ^oC.[35] This fact can be explained by the different charge density of the host layer of the layered titanates, which increases in an order of $H_{1.07}Ti_{1.73}O_4$ < $H_2Ti_4O_9$ < $H_2Ti_3O_7$. The layered structures are held by attracting between the negatively charged host layers and the positively charged H^+ or H_3O^+ ions in the interlayer spaces. The attraction between the host layers and interlayer ions enhances with increasing the charge density. Therefore, the higher charge density, it is more difficult to be interlayered and exfoliated into the nanosheets. When the TMA^+-$H_2Ti_3O_7$ (TMA-HTO) sample is dispersed in distilled water, the layered structure is exfoliated into nanosheets, resulting a TMA-HTO nanosheet colloidal solution.

Figs. 2(a, b) show the typical SEM images of the $Na_2Ti_3O_7$ and $H_2Ti_3O_7$ samples. The $Na_2Ti_3O_7$ sample exhibits rodlike particle morphology with a size of about 10 μm in length and 2 μm in width. After ion-exchange reaction, the $H_2Ti_3O_7$ sample maintains the rodlike particle morphology. The axis-direction of the rodlike $H_2Ti_3O_7$ particles corresponds to *b*-axis direction (Fig. 2(c)).[38, 39] Figs. 2(d-f) show the HR-TEM images and SAED pattern of TMA-HTO nanosheet sample. After the exfoliation treatment, the particle morphology changes to nanosheetlike morphology. In the SAED pattern of the nanosheet sample, (020) and (003) diffractions are observed, the HR-TEM images also accord with the result of SAED patterns, which is indicated the basal plane of the HTO nanosheet is parallel to *b*- and *c*-axis, namely the

10

exfoliation occurs along *a*-axis direction.

3.2 Synthesis of TiO₂ nanocrystals from TMA-HTO nanosheet colloidal solution

The prepared TMA-HTO nanosheet colloidal solutions were hydrothermally treated to synthesize TiO₂ nanocrystals. The XRD patterns of the products prepared under various temperature and pH conditions are shown in Fig. S1 in the Supplementary Information. The dependence of the products on the hydrothermal reaction conditions is summarized in Fig. 3. In a range of pH < 1, rutile, anatase, brookite phases can be formed, and the percentages of brookite and anatase phases decrease gradually with increasing the hydrothermal reaction temperature. The brookite phase disappears over 170 ^{o}C, and anatase phase disappears over 200 ^{o}C. This result reveals that the stability increases in an order of brookite < anatase < rutile under the acidic conditions of pH < 1. The single anatase phase can be obtained in a wide pH range of 1 < pH < 12. The crystallinity of anatase phase increases with increasing of the temperature and pH value (see Fig. S2 in the Supplementary Information). The percentage of the TMA-HTO layered phase decreases with increasing of the temperature at the same pH value (see Fig. S1 in the Supplementary Information), and the TMA-HTO nanosheets are transformed completely to anatase phase over 180 ^{o}C in this pH range (Fig. 3). Furthermore, the EDS analysis results reveal that without sodium residual in the synthesized TiO₂ samples (see Fig. S3 in the Supplementary Information).

Fig. 4 shows the FE-SEM images of the products obtained by hydrothermal treatment of the TMA-HTO nanosheets. At 160 ^{o}C-pH 0.65, the main particles are nanorod-like particles with a size of about 50 nm in length and 20 nm in width, and some large rod-like particles with a size of about 500 nm in length and 50 nm in width, are observed also (Fig. 4(a)). The nanorod-like particles and the large rod-like particles can be assigned to anatase and rutile phases, respectively, because the XRD

11

result indicates that the sample contains anatase main phase and small amount of rutile (see Fig. S1(c) in the Supplementary Information). At 170 ^{o}C-pH 0.65, the main rod-like particles with size of about 500 nm in length and 100 nm in width and small amount of small nanoparticles with size of about 20 nm are observed (Fig. 4(b)). The rod-like particles correspond to rutile phase because the XRD result indicates that the main phase is rutile (see Fig. S1(d) in the Supplementary Information). The size of rutile particles increases with increasing the reaction temperature, and become about 1 μm in length at 200 ^{o}C-pH 0.65 (Fig. 4(c)). The result suggests that the rutile phase is formed by a dissolution-deposition reaction under the low pH conditions.[40-42]

Around pH 3, TMA-140-3.2 sample is a mixture of anatase and layered phases, and shows nanorod-like particles with a size of about 50 nm in length and 20 nm in width and nanosheet-like particles (Fig. 4(d)). The nanorod-like and nanosheet-like particles can be assigned to anatase and layered phases, respectively. The nanosheet-like particles disappear, and nanorod-like particles of anatase are formed in TMA-160-2.3 sample (Fig. 4(e)). The nanorod-like particles of anatase tend to change to tetragonal nanoparticles with increasing the reaction temperature to 200 ^{o}C around pH 3 (Fig. 4(f)).

Around pH 7, TMA-140-7.9 sample containing the layered and anatase phases shows nanosheet-like particles, tetragonal particles and nanorod-like particles (Fig. 4(g)). Tetragonal nanoparticles of anatase with a size about 100 nm are formed in TMA-170-7.3 sample (Fig. 4(h)). At 180 ^{o}C and 200 ^{o}C, the nanorod-like anatase TiO_2 particles with a size about 100 nm in length and 50 nm in width are formed (Fig. 4(i, j)).

In TMA-150-12 sample, nanosheet-like particles of the layered phase and nanoleaf-like particles of anatase phase with a size about 500 nm in length and 50 nm in width are observed (Fig. 4(k)), and the nanoleaf-like particles of anatase phase are

12

also observed in TMA-200-11.6 sample (Fig. 4(l)). The above results reveal that the particle morphology of anatase is strongly dependent on the hydrothermal reaction temperature and pH value of the reaction solution, which is similar to the cases of hydrothermal reactions of the lepidocrocite-like $H_{1.07}Ti_{1.73}O_4$ and $H_2Ti_4O_9$ layered titanate nanosheets.[33-35]

3.3 Nanostructural study of TiO$_2$ nanocrystals and transformation reaction mechanism from TMA-HTO nanosheets to TiO$_2$ nanocrystals

The nanostructures of TiO$_2$ nanocrystals and their formation mechanism from TMA-HTO nanosheets were studied using TEM. Fig. 5 shows the TEM images and fast Fourier Transform (FFT) diffraction pattern of the TMA-140-3.2 sample containing the HTO layered and anatase phases. A nanosheet-like particle shows the (003) and (010) diffraction spots of HTO layered phase, and also the (101) and (011) diffraction spots of anatase phase in the FFT diffraction. This nanosheet-like particle is an intermediate product of topochemical transformation reaction from the layered phase to the anatase phase. There is a specific crystallographic relationship between the layered structure and anatase structure in the topochemical structural transformation reaction as shown in Fig. 5(d). The (100)-facet of the layered phase corresponds to a facet vertical to [111]-direction of anatase structure and these facets are parallel to the basal plane of the nanosheet-like particle. The [010] orientation of the layered phase is transformed to the [101] orientation of anatase phase by rotating an angle of 20° on the basal plane of the nanosheet-like particle (Fig. 5(c)). This topochemical reaction causes formation anatase nanosheet with a crystal facet vertical to [111]-direction on the nanosheet-like surface. We call it [111]-faceted anatase nanocrystal. The [111]-facet is different from {111}-facet in the tetragonal system of anatase phase.[34, 35, 43]

The TEM images and FFT diffraction patterns of TiO_2 nanocrystals synthesized from TMA-HTO are shown in Fig. 6. In the TMA-160-0.65 sample, rod-like crystal shows lattice fringes with *d*-values of 0.32 and 0.25 nm in TEM image and its diffraction spots in FFT pattern, which correspond to (110) and (101) planes of rutile phase, respectively (Fig. 6(a)). This result indicates that the rod-like crystals correspond to rutile phase, the two side faces of the rod-like crystal correspond to {110} facet. In the TMA-200-0.65 sample, rod-like crystal shows rutile lattice fringes of (110) plane with *d*-values of 0.32 and (111) plane with *d*-value of 0.22 nm in TEM image and the corresponding diffraction spots in FFT pattern (Fig. 6(b, c)), indicating that the two side faces also correspond to (110) facet of rutile.

In TMA-160-2.3 sample, main particles are nanorod-like anatase particles. These nanocrystals exhibit the lattice fringes of (101) and (011) planes with a *d*-value of 0.35 nm (Fig. 6(d)). This result reveals that the four side faces of nanorod correspond to {101} facet and the basal plane to [111]-facet. The nanorod-like anatase particles in TMA-200-3.6 sample also show the lattice fringes and the diffraction spots of (101) and (011) planes with a *d*-value of 0.35 nm (Fig. 6(e)). The above results suggest that [111]-faceted anatase nanocrystals are formed mainly from the TMA-HTO nanosheets around pH 3 under hydrothermal conditions. A few of rhombic and hexagonal anatase TiO_2 nanocrystals with {010} facet on the surfaces were observed also around pH 3 (see Fig. S4 in the Supplementary Information).

In TMA-170-7.3 sample, the main particles are anatase tetragonal nanocrystals which have [111]-facet on the surface (Fig. 6(f)). In TMA-200-6.7 sample, the nanorod-like anatase nanocrystals exhibit lattice fringes with *d*-values of 0.35 nm and 0.46 nm, respectively, corresponding to (101) and (002) planes in its HR-TEM image and its FFT diffraction pattern (Fig. 6(g)). The result reveals that the basal plane of nanorod-like anatase TiO_2 nanocrystals correspond to a (010)-facet, and other two

14

side faces correspond to (100)-facet. The long-axis direction of the nanorod corresponds to [001] direction. These results suggest that at around pH7, the [111]-faceted anatase nanocrystals are formed preferentially at low temperature, and {010}-faceted anatase nanocrystals are formed preferentially at high temperatures.

At around pH 12, the typical nanoleaf-like nanocrystals are obtained. Which exhibit lattice fringes with a *d*-value of 0.35 nm corresponding to (101) plane and (-101) plane of anatase phase (Fig. 6(h)), and *d*-values of 0.35 nm and 0.48 nm corresponding to (101) plane and (002) plane of anatase phase (Fig. 6(i)) in HR-TEM images. The result reveals the nanoleaf-like anatase nanocrystals expose {010}-facet on the basal plane. Furthermore, the long-axis and width-axis of the nanoleaf-like nanocrystal along with [001] orientation and [100] orientation, respectively.

On the basis of the results described above, we give a reaction mechanism for the transformation of TMA-HTO nanosheets to TiO_2 under the hydrothermal conditions as shown in Fig. 7. The structure and particle morphology of TiO_2 are strongly dependent on pH value of the reaction solution and reaction temperature. The rutile phase with rod-like morphology is formed under low pH conditions of pH < 1 by dissolution-decomposition reaction, due to higher solubility of TiO_2 under the low pH conditions.[17] Around pH 3, the TMA-HTO nanosheets are transformed firstly to [111]-faceted nanosheet-like anatase particles by the topochemical reaction (Fig. 5). And then the nanosheet-like anatase particle is split into nanorod-like anatase particles by dissolution reaction along {101}-facet. The formed nanorod-like anatase particles have basal plane corresponding to [111]-facet and four side faces corresponding to {101}-facet. At around pH 7 and low temperature, similar reactions to those at pH 3 occur, and then tetragonal anatase nanoparticles with basal plane corresponding to [111]-facet and four side faces to {101}-facet.

Around pH 12, we think that the TMA-HTO nanosheets are transformed firstly to

15

{010}-faceted nanosheet-like anatase particles by the topochemical reaction.[34, 35] And then the nanosheet-like anatase particle is split into nanoleaf-like anatase particles by dissolution reaction along (100)-facet. The formed nanosheet-like anatase particles have basal plane corresponding to {010}-facet and long-axis corresponding to [001]-direction. The reactions at around pH 7 and high temperatures are the same as the reactions occur at pH 12. Namely the TMA-HTO nanosheets are transformed firstly to {010}-faceted nanosheet-like anatase particles, and then the {010}-faceted nanosheet-like anatase particles are split into nanorod-like anatase nanoparticles with a basal plane and two side faces corresponding to {010}-facet, and a long-axis corresponding to the [001]-direction.

The results described above reveal that the anatase nanocrystals with different facets on their surfaces can be obtained under different pH and temperature conditions, and two kinds of typical facets exposed on anatase nanocrystal surface can be obtained. One is {010}-faceted, and another is [111]-faceted anatase nanocrystals. The results are similar to formation of the anatase nanocrystals from tetra-titanate nanosheets under hydrothermal conditions in our previous study.[35] The formation of these two kinds of typical facets exposed on anatase nanocrystal surface can be explained by splitting the layered titanate nanosheets along different facets under different pH conditions. The splitting along {001}-facet of HTO nanosheet causes formation of the [111]-faceted anatase nanoparticles, while that along the {010}-facet of HTO nanosheet causes formation of the {010}-faceted anatase nanoparticles.[35]

The above results also revealed that the TiO_2 nanocrystals can be formed from TMA-HTO nanosheets by two kinds of simultaneous reactions.[17, 32, 33] One is the in situ topochemical conversion reaction, which transforms the layered structure of TMA-HTO nanosheets to the anatase TiO_2 structure. Another is the dissolution-deposition reaction, which transforms the nanosheet-like particle

16

morphology to other nanoparticle morphology. Therefore, controlling the dissolution-deposition reaction is significant to control the particle morphology and size.

3.4 Electronic band structure and photocatalytic activity of TiO₂ nanocrystals

To study crystal facets effect on the photocatalytic activity of TiO_2 nanocrystals, the photocatalytic degradations of methylene blue (MB) dye by TiO_2 nanocrystals were measured under UV-light irradiating conditions. In the photocatalytic study, two anatase nanocrystal samples with uniform crystal morphology, TMA-200-3.6 ([111]-faceted anatase nanorods, Fig. 4(f)) and TMA-200-6.7 ({010}-faceted anatase nanorods, Fig. 4(g)), and a rutile nanocrystal sample of TMA-200-0.65 (nanorods, Fig. 4(c)) are chosen to compare with commercial P25 TiO_2 nanocrystal sample as the standard sample. The P25 sample is a well-known highly active photocatalytic TiO_2 sample, which contains 80% anatase phase with a particle size of about 20 nm and 20% rutile phase with a particle size of about 80 nm, where half of anatase is the [111]-faceted tetragonal nanocrystal and other half is the sphere nanocrystal without a specific facet on the surface.[34, 43] Furthermore, an anatase nanocrystal sample of ST20 with particle size of about 20 nm and a spherical particle morphology was used also as a standard sample without a specific facet on the surface. The BET specific surface area, and particle size of these TiO_2 samples are shown in Table 1. To understand the facet effect on the photocatalytic activity easily, the facet proportions exposed on the surface for the samples with specific facet were estimated based on their crystal morphologies (Fig. 4) and results of the nanostructural studies (Fig. 6). The result suggests that TMA-200-6.7, TMA-200-3.6, and P25 contain 85% of {010}-facet, 43% of [111]-facet, and 22% of [111]-facet, respectively.

The results of photocatalytic degradation of MB reveal that photocatalytic activity

17

(mg/g) increases in an order of TMA-200-0.65 < ST20 < TMA-200-6.7 < TMA-200-3.6 < P25 in Fig. 8(a). The P25 and TMA-200-0.65 exhibit the highest and the lowest photocatalytic activities, respectively in these samples. It is well-known that the photocatalytic activity is strongly dependent on the surface area of TiO_2 because the photocatalytic reaction occurs on the TiO_2 surface, and also anatase phase exhibits higher photocatalytic activity than that of the rutile phase.[44, 45] The low photocatalytic activity of TMA-200-0.65 is due to its small surface area and rutile phase. The surface area of the anatase samples increase in an order of TMA-200-6.7 < TMA-200-3.6 < P25 < ST20, which does not corresponds to the increasing order of the photocatalytic activity. We think this difference can be explained by different photocatalytic activities of the different crystal facets exposing on the TiO_2 surface. To understand the surface photocatalytic activity, we evaluated the MB degradation amount by per surface area of TiO_2 sample (mg(MB)/m^2(TiO_2 surface area)), and the result is shown in Fig. 8(b). Therefore, the surface photocatalytic activity (mg/m^2) increases in an order of TMA-200-0.65 < ST20 < P25 < TMA-200-3.6 < TMA-200-6.7. By considering the facet proportions exposed on the surface, this result suggest that the surface photocatalytic activity increases in an order of rutile < anatase (non-facet) < anatase ([111]-facet) < anatase ({010}-facet).

Furthermore, we study the surface electronic band structures of the TiO_2 nanocrystals in order to explain the surface photocatalytic activity. The UV-visible absorption spectra of TiO_2 samples are shown in Fig. 9(a). Because of the TiO_2 is an indirect semiconductor, the relation between absorption coefficient (***A***) and incident photon energy (***hv***) can be represented as Kubelka-Munk function $A = B(hv-E_g)^2/hv$, where ***B*** and E_g are the absorption constant and bandgap energy.[46] The bandgap energy can be estimated from transformed Kubelka-Munk function versus the energy of light (Fig. 9(b)),[26, 47] and the results are shown in Table 1. The bandgap increases in

18

an order of TMA-200-0.65 < ST20 < P25 < TMA-200-3.6 < TMA-200-6.7, which corresponds to the increasing order of surface photocatalytic activity. The different bandgap values can be attributed to their different crystal phases and exposed facets on the particle surface.[24-26] Namely, the rutile phase sample has smaller bandgap than anatase phase samples.[48] In the anatase samples, the bandgap increases in an order of ST20 (non-facet) < P25 (22%-[111]-facet) < TMA-200-3.6 (43%-[111]-facet) < TMA-200-6.7 (85%-{010}-facet), namely non-facet < [111]-facet < {010}-facet. The result reveals that the bandgap is dependent on the facet on the surface.[47]

Basis on the bandgap results described above and the energy level of the highest valence band reported, we illustrate the band structures of these TiO_2 nanoparticle sample in Fig. 9(c). The literature values of -7.1 eV and -7.5 eV are used as the highest valence band level for rutile [49] and anatase [50] phases, respectively. It has been reported that the energy levels of the highest valence band of anatase nanocrystals are almost independent on their crystal size and the facet on the surface.[24-26] Therefore, the same value (-7.5 eV) of the highest valence band is used for all anatase nanocrystal samples. Although P25 is a mixed phase of anatase and rutile, -7.1 eV is used as the highest valence band value for P25, because its principal component (80%) is anatase and anatase exhibits higher photocatalytic activity than that of rutile, furthermore it would be reasonable to use the energy level of the highest valence band of anatase for P25 photocatalytic study.

The result reveals that the lowest energy level of the conduction band increases in an order of ST20 (non-facet) < P25 (22%-[111]-facet) < TMA-200-3.6 (43%-[111]-facet) < TMA-200-6.7 (85%-{010}-facet) for the anatase samples. This result suggests that energy level of lowest conduction band of anatase increases in an order of non-facet < [111]-facet < {010}-facet. In the photocatalytic reaction, the TiO_2 nanocrystals with a higher energy level of the lowest conduction band can generate

19

more strongly reductive electrons for the photocatalytic reaction, meaning stronger reduction ability and superior photocatalytic activity. Hence, the surface electronic band structure of the {010}-faceted anatase can provide high potential electrons for the reduction reaction. Although the rutile sample (TMA-200-0.65) has a higher energy level of lowest conduction band than the anatase samples, but its energy level of highest valence band is also higher than that of the anatase samples. The higher energy level of the highest valence band will show weaker oxidation ability in the photocatalytic reaction.[14]

3.5 DSSC Performance of [111]-faceted TiO$_2$ Nanocrystals

In our previous studies, it has found that the DSSC performance is dependent the facet of anatase nanocrystals, which increases in an order of non-facet (ST20) < [111]-facet (P25) < {010}-facet of anatase nanocrystals.[34, 43] To confirm the DSSC performance of the [111]-faceted anatase nanocrystal, we investigated the DSSC performance of [111]-faceted anatase sample of TMA-200-3.6 and compared with that of P25 because they have similar particle size and the particle size of about 30 nm is suitable for DSSCs. The cell parameters and *I-V* characteristics of DSSCs cells fabricated using TMA-200-3.6 and P25 with the similar thickness of porous TiO$_2$ film are given in Table 2 and in Fig. S5 in the Supplementary Information. TMA-200-3.6 exhibits larger J_{sc} and V_{oc} values (11.9 mA/cm^2 and 0.67 V) than which (11.5 mA/cm^2 and 0.61 V) of P25, and almost the same *ff* value (0.6), resulting larger η value of TMA-200-3.6 than that of P25. The result suggests that the DSSC performance (η) enhances in the order of non-facet < [111]-facet < {010}-facet. The increasing order corresponds to the increasing orders of the bandgap and the lowest energy level of conduction band (Figure 9(c)). We also confirmed that crystal morphology and facet of the anatase nanocrystals did not change after calcination treatment in the

20

fabrication process of TiO$_2$ electrode by FE-SEM and TEM analyses (see Fig. S5 and Fig. S6 in the Supplementary Information).

The different DSSCs performances may be due to different dye adsorption behavior on the different facets. It has been reported the N719 dye adsorption constant K_{ad} on anatase nanocrystal surface increases in an order of non-facet < [111]-facet < {010}-facet,[35] namely the strong adsorption of the dye molecules onto the TiO$_2$ surface can enhance η value. [51-53] The dye molecules can be anchored more strongly on [111]-faceted anatase nanocrystal surface of TMA-200-3.6 than that on P25 nanocrystal surface, and the strong anchoring can improve the injection rate of photogenerated electrons from the dye molecules into the conduction band of TiO$_2$, which can enhance J_{sc}.[34, 51]

4. Conclusions

The various TiO$_2$ nanocrystals with controllable crystal phase, crystal size and particle morphology can be synthesized from the TMA-HTO nanosheets by hydrothermal treatment. The phases, sizes and morphologies of the TiO$_2$ nanocrystals strongly depend on the reaction temperature and pH value of the reaction solutions. The [111]-faceted and {010}-faceted anatase TiO$_2$ nanocrystals are formed by two kinds of reactions in the reaction process. One is the in situ topochemical conversion reaction from the TMA-HTO layered structure to anatase structure, and another is the dissolution-deposition reaction on the particle surface, which splits the nanosheet-like particles to small nanocrystals. The [111]-faceted anatase nanocrystals are formed preferentially under lower pH and lower temperature conditions than which of {010}-faceted anatase nanocrystals. The anatase nanocrystals exhibit higher surface photocatalytic activity than that of rutile nanocrystals. Furthermore, the surface photocatalytic activity of anatase nanocrystals are dependent on the facet exposing on

the particle surface, which enhances in the order of non-facet < [111]-facet < {010}. The increasing order corresponds to the increasing order of the bandgap and the energy level of lowest valence band of the anatase nanocrystals. The facet of anatase also affects the DSSCs performance, which enhances in the order non-facet < [111]-facet < {010}-facet. The results suggest that the facet on the surface is important factor to improve the photocatalytic activity and the DSSCs performance.

Associated Content

Electronic Supplementary Information

XRD patterns of products obtained by hydrothermal treatment in the temperature range of 140-200 ^{o}C, dependences of the (101) peak intensity of anatase on the pH values of nanosheet solution at different temperature, EDS analysis results of synthesized TiO_2 samples, TEM images and FFT diffraction pattern of TMA-150-2.5 sample, *I-V* characteristics and FE-SEM images in cross-section of the TiO_2-film electrodes of DSSCs cells fabricated using TMA-200-3.6 and P25 samples, TEM images of TMA-200-3.6 anatase nanocrystal samples after the calcination at 480 ^{o}C for 1h. This material is available free of charge via the Internet at http://pubs.rsc.org/.

Acknowledgements

.

References

22

Nanoscale Accepted Manuscript

1 A. Fujishima and K. Honda, *Nature*, 1972, **238**, 37-38.

2 A. Fujishima, T. N. Rao and D. A. Tryk, *J. Photoch. Photobio. C*, 2000, **1**, 1-21.

3 B. O'Regan and M. Grätzel, *Nature*, 1991, **335**, 737-740.

4 M. Grätzel, *Prog. Photovolt. Res. Appl.*, 2000, **8**, 171-185.

5 M. Grätzel, *J. Photoch. Photobio. C*, 2003, **4,** 145-153.

6 J. H. Liu, J. S. Chen, X. F. Wei, X. W. Lou and X. W. Liu, *Adv. Mater.*, 2011, **23**, 998-1002.

7 T. Miyata, S. Tsukada and T. Minami, *Thin Solid Films*, 2006, **496**, 136-140.

8 Y. X. Leng, J. Y. Chen, H. Sun, P. Yang, G. J. Wan, J. Wang and N. Huang, *Surf. Coat. Tech.*, 2004, **176**, 141-147.

9 W. Tang, *J. Mater. Chem.*, 2004, **14**, 3457-3461.

10 D. M. Antonelli and J. Y. Ying, *Angew. Chem. Int. Edit.*, 1995, **34**, 2014-2017.

11 H. Cheng, J. Ma, Z. Zhao and L. Qi, *Chem. Mater.*, 1995, **7**, 663-671.

12 A. Chemseddine, H. Jungblut and S. Boulmaaz, *J. Phys. Chem.*, 1996, **100**, 12546-12551.

13 R. L. Whetten, J. T. Khoury, M. M. Alvarez, S. Murthy, I. Vezmar, Z. L. Wang, P. W. Stephens, C. L. Cleveland, W. D. Luedtke and U. Landman, *Adv. Mater.*, 1996, **8**, 428-433.

14 A. L. Linsebigler, G. Lu and J. T. Yates Jr., *Chem. Rev.*, 1995, **95**, 735-758.

15 U. Diebold, *Surf. Sci. Rep.*, 2003, **48**, 53-229.

16 X. Q. Gong, A. Selloni, M. Batzill and U. Diebold, *Nat. Mater.*, 2006, **5**, 665-670.

17 P. Wen, H. Itoh, W. Tang and Q. Feng, *Lamgmuir*, 2007, **23**, 11782-11790.

18 H. G. Yang, C. H. Sun, S. Z. Qiao, J. Zou, G. Liu, S. C. Smith, H. M. Cheng and G. Q. Lu, *Nature*, 2008, **453**, 638-641.

19 B. Wu, C. Guo, N. Zheng, Z. Xie G. D. Stucky, *J. Am. Chem. Soc.*, 2008, **130**, 17563-17567.

20 X. Han, Q. Kuang, M. Jin, Z. Xie and L. Zheng, *J. Am. Chem. Soc.*, 2009, **131**, 3152-3153.

21 F. Amano, T. Yasumoto, O. O. Prieto-Mahaney, S. Uchida, T. Shibayama and B. Ohtani, *Chem. Commun.*, 2009, **17**, 2311-2313.

22 G. Liu, C. Sun, H. G. Yang, S. C. Smith, L. Wang, G. Q. Lu and H. M. Cheng, *Chem. Commun.*, 2010, **46**, 755-757.

23 J. Yu, Q. Xiang, J. Ran and S. Mann, *CrystEngComm*, 2010, **12**, 872-879.

24 J. Pan, G. Liu, G. Lu and H. Cheng, *Angew. Chem. Int. Ed.*, 2011, **50**, 2133-2137.

25 J. Pan, X. Wu, L. Wang, G. Liu, G. Lu and H. Cheng, *Chem. Commun.*, 2011, **47**, 8361-8363.

26 H. Xu, S. Ouyang, P. Li, T. Kako and J. Ye, *ACS Appl. Mater. Interfaces*, 2013, **5**, 1348-1354.

27 L. Shen, N. Bao, Y. Zheng, A. Gupta, T. An and K. Yanagisawa, *J. Phys. Chem. C*, 2008, **112**, 8809-8818.

28 J. Yu, J. Fan and K. Lv, *Nanoscale*, 2010, **2**, 2144-2149.

29 M. Liu, L. Piao, L. Zhao, S. Ju, Z. Yan, T. He, C. Zhou and W. Wang, *Chem. Commun.*, 2010, **46**, 1664-1666.

30 J. Li and D. Xu, *Chem. Commun.*, 2010, **46**, 2301-2303.

31 P. Wen, H. Itoh, Q. Feng, *Chem. Lett.*, 2006, **35**, 1226-1227.

32 P. Wen, H. Itoh, W. Tang and Q. Feng, *Microporous Mesoporous Mat.*, 2008, **116**, 147-156.

33 P. Wen, Y. Ishikawa, H. Itoh and Q. Feng, *J. Phys. Chem. C*, 2009, **113**, 20275-20280.

34 C. Chen, G. A. Sewvandi, T. Kusunose, Y. Tanaka, S. Nakanishi and Q. Feng, *CrystEngComm*, 2014, **16**, 8885-8895.

35 Y. Du, Q. Feng, C. Chen, Y. Tanaka and X. Yang, *ACS Appl. Mater. Interfaces*,

2014, **6**, 16007-16019.

36 M. Qamar, C.R. Yoon, H. J. Oh, N. H. Lee, K. Park, D. H. Kim, K. S. Lee, W. J. Lee and S. J. Kim, *Catal. Today*, 2008, **131**, 3-14.

37 P. Gao, D. Bao, Y. Wang, Y. Chen, L. Wang, S. Yang, G. Chen, G. Li, Y. Sun and W. Qin, *ACS Appl. Mater. Interfaces*, 2013, **5**, 368-373.

38 S. Papp, L. Kõrösi, V. Meynen, P. Cool, E. F. Vansant and I. Dékány, *J. Solid State Chem.*, 2005, **178**, 1614-1619.

39 K. Kataoka, N. Kijima and J. Akimoto, *Inorg. Chem.*, 2013, **52**, 13861-13864.

40 Y. Zheng, E. Shi, Z. Chen, W. Li and X. Hu, *J. Mater. Chem.*, 2001, **11**, 1547-1551.

41 X. Feng, J. Zhai and L. Jiang, *Angew. Chem. Int. Ed.*, 2005, **44**, 5115-5118.

42 G. Li and K. A. Gray, *Chem. Mater.*, 2007, **19**, 1143-1146.

43 C. Chen, L. Xu, G. A. Sewvandi, T. Kusunose, Y. Tanaka, S. Nakanishi and Q. Feng, *Cryst. Growth Des.*, 2014, **14**, 5801-5811.

44 L. Liu, H. Zhao, J. M. Andino and Y. Li, *ACS Catal.*, 2012, **2**, 1817-1828.

45 T. Luttrell, S. Halpegamage, J. Tao, A. Kramer, E. Sutter and M. Batzill, *Sci. Rep.*, 2014, **4**, 4043.

46 M. A. Butler, *J. Appl. Phys.*, 1977, **48**, 1914-1920.

47 H. Xu, P. Reunchan, S. Ouyang, H. Tong, N. Umezawa, T. Kako and J. Ye, *Chem. Mater.*, 2013, **25**, 405-411.

48 V. E. Henrich and R. L. Kurtz, *Phys. Rev. B*, 1981, **23**, 6280-6287.

49 D. O. Scanlon, C. W. Dunnill, J. Buckeridge, S. A. Shevlin, A. J. Logsdail, S. M. Woodley, C. R. A. Catlow, M. J. Powell, R. G. Palgrave, I. P. Parkin, G. W. Watson, T. W. Keal, P. Sherwood, A. Walsh and A. A. Sokol, *Nat. Mater.*, 2013, **12**, 798-801.

50 R. Nakamura, T. Tanaka and Y. Nakato, *J. Phys. Chem. B*, 2004, **108**, 10617-10620.

51 P. Wen, M. Xue, Y. Ishikawa, H. Itoh and Q. Feng, *ACS Appl. Mater. Interfaces.*, 2012, **4**, 1928-1934.

52 P. Wen, Z. Tao, Y. Ishikawa, H. Itoh and Q. Feng, *Appl. Phys. Lett.*, 2010, **97**, 131906.

53 G. A. Sewvandi, C. Chen, T. Ishii, T. Kusunose, Y. Tanaka, S. Nakanishi and Q. Feng, *J. Phys. Chem. C*, 2014, **118**, 20184-20192.

Table 1. Crystal phase, Exposed facet, Surface area, Crystal size, and Bandgap energy for TMA-200-0.65, TMA-200-3.6, TMA-200-6.7, ST20, and P25 samples.

Sample	*Crystal phase*	*Exposed facet (Anatase)*	S_{BET} *(m²/g)*	*Crystal size (nm)*	*Eg (eV)*
P25	Anatase (80%)	[111]	52.6	20 (Anatase)	3.04
	Rutile (20%)	None		80 (Rutile)	
ST20	Anatase	None	66.4	20	3.01
TMA-200-0.65	Rutile	----	26.9	100×500 (width×length)	2.95
TMA-200-3.6	Anatase	[111]	44.7	50	3.07
TMA-200-6.7	Anatase	{010}	32.0	30×150 (width×length)	3.14

Table 2. Cell parameters of DSSCs fabricated using TMA-200-3.6 and P25 samples.

Sample	Thickness (μm)	J_{sc} (mA/cm^2)	V_{oc} (V)	ff	η (%)
TMA-200-3.6	8.4	11.9	0.67	0.61	4.84
P25	7.9	11.5	0.61	0.57	4.05

Figure Captions

Fig. 1 XRD patterns of (a) $Na_2Ti_3O_7$, (b) $H_2Ti_3O_7$, and (c) TMA^+-form $H_2Ti_3O_7$ (TMA-HTO) samples.
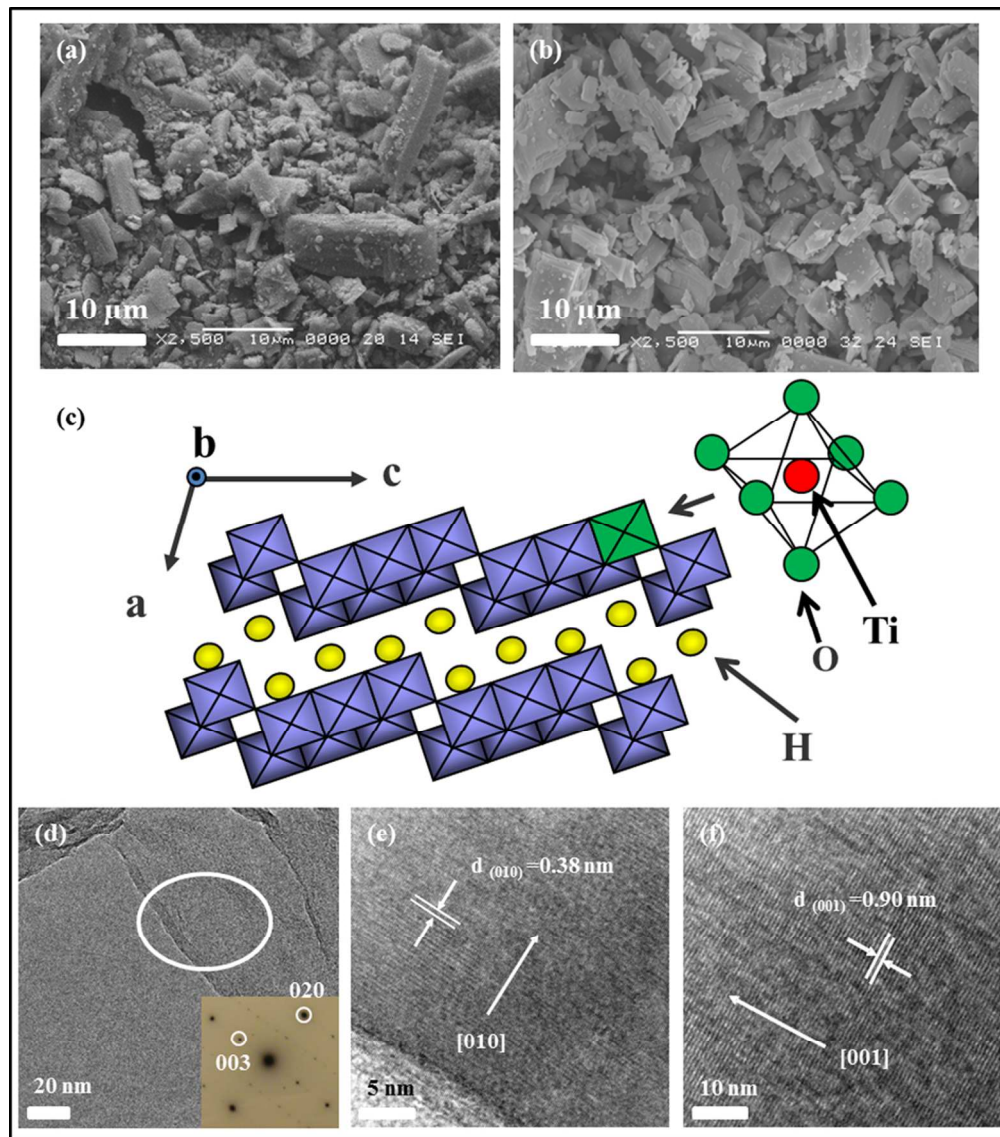
Fig. 2 SEM image of (a) $Na_2Ti_3O_7$ and (b) $H_2Ti_3O_7$ sample, (c) crystal structure of $H_2Ti_3O_7$, (d) TEM image and SAED pattern of TMA-HTO nanosheet sample, and (e, f) HR-TEM images of TMA-HTO nanosheet sample.

Fig. 3 Dependence of the products on the reaction temperature and the pH value, ○: anatase, ●: rutile, △: anatase+rutile, ■: layered titanate+anatase, ▲: anatase+rutile+brookite.

Fig. 4 FE-SEM images of (a) TMA-170-0.65, (b) TMA-170-0.56, (c) TMA-200-0.65, (d) TMA-140-3.2, (e) TMA-160-2.3, (f) TMA-200-3.6, (g) TMA-140-7.9, (h) TMA-170-7.3, (i) TMA-180-6.9, (j) TMA-200-6.7, (k) TMA-150-12, and (l) TMA-200-11.6 samples.

Fig. 5 (a, b) TEM images and (c) FFT diffraction patterns of TMA-140-3.2 sample, and (d) structure transformation from layered structure to anatase structure.

Fig. 6 TEM images and FFT diffraction patterns of (a) TMA-160-0.65, (b, c) TMA-200-0.65, (d) TMA-160-2.3, (e) TMA-200-3.6, (f) TMA-170-7.3, (g) TMA-200-6.7, (h) TMA-150-12, and (i) TMA-200-11.6 samples.

Fig. 7 Transformation reaction mechanism from TMA-HTO nanosheets to TiO_2

nanocrystals.

Fig. 8 Photocatalytic degradations of methylene blue (MB) by TMA-200-0.65 (rutile), TMA-200-3.6 ([111]-faceted anatase), TMA-200-6.7 ({010}-faceted anatase), P25 (partially [111]-faceted anatase), and ST20 (non-faceted anatase) samples presented by (a) mg(MB)/g(TiO$_2$) and (b) mg(MB)/m^2(TiO$_2$), respectively.

Fig. 9 (a) UV-visible absorption spectra; (b) the corresponding plots of transformed Kubelka-Munk function versus the energy of photon; (c) schematic illustration of the electronic band alignments of (I) TMA-200-0.65 (rutile), (II) ST20 (non-faceted anatase), (III) P25 (partially [111]-faceted anatase), (IV) TMA-200-3.6 ([111]-faceted anatase) and (V) TMA-200-6.7 ({010}-faceted anatase) samples.

Figure for TOC. Topochemical conversion of H$_2$Ti$_3$O$_7$ nanosheet to morphology controllable [111]-faceted and {010}-faceted anatase TiO$_2$ nanocrystals.
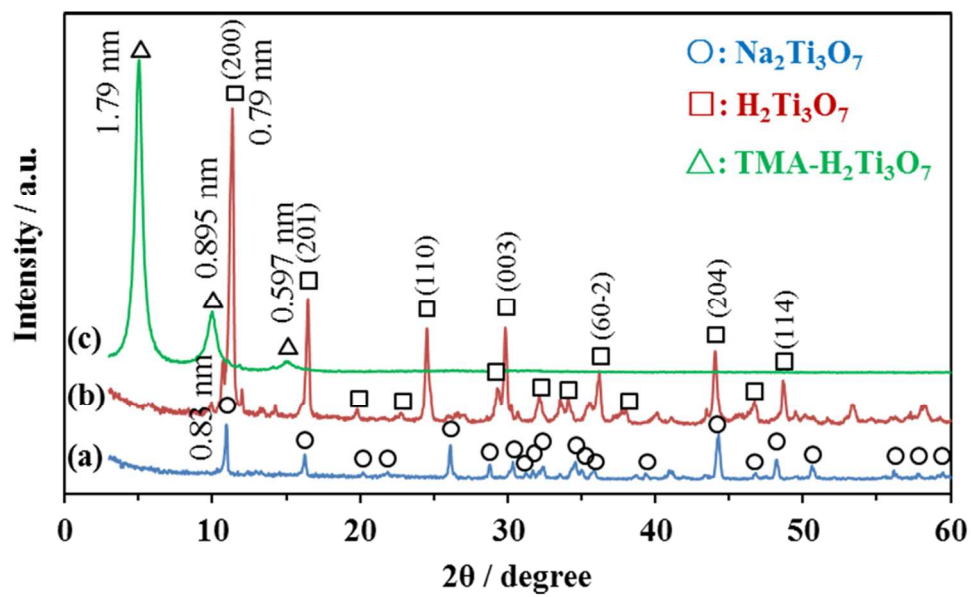
Fig. 1 XRD patterns of (a) Na2Ti3O7, (b) H2Ti3O7, and (c) TMA+-form H2Ti3O7 (TMA-HTO) samples.
82x52mm (300 x 300 DPI)

Fig. 2 SEM image of (a) Na2Ti3O7 and (b) H2Ti3O7 sample, (c) crystal structure of H2Ti3O7, (d) TEM image and SAED pattern of TMA-HTO nanosheet sample, and (e, f) HR-TEM images of TMA-HTO nanosheet sample.
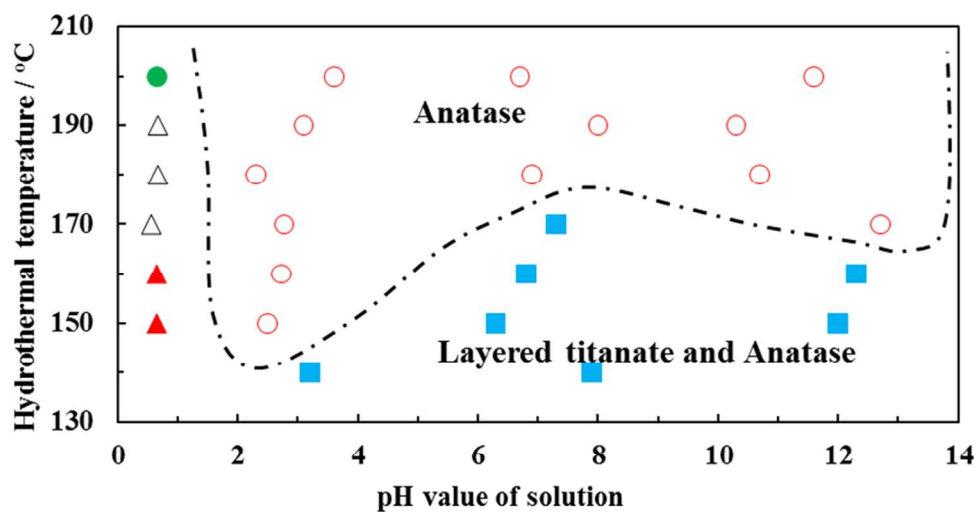82x94mm (300 x 300 DPI)

Fig. 3 Dependence of the products on the reaction temperature and the pH value, ○: anatase, ●: rutile, △: anatase+rutile, ■: layered titanate+anatase, ▲: anatase+rutile+brookite.
82x45mm (300 x 300 DPI)
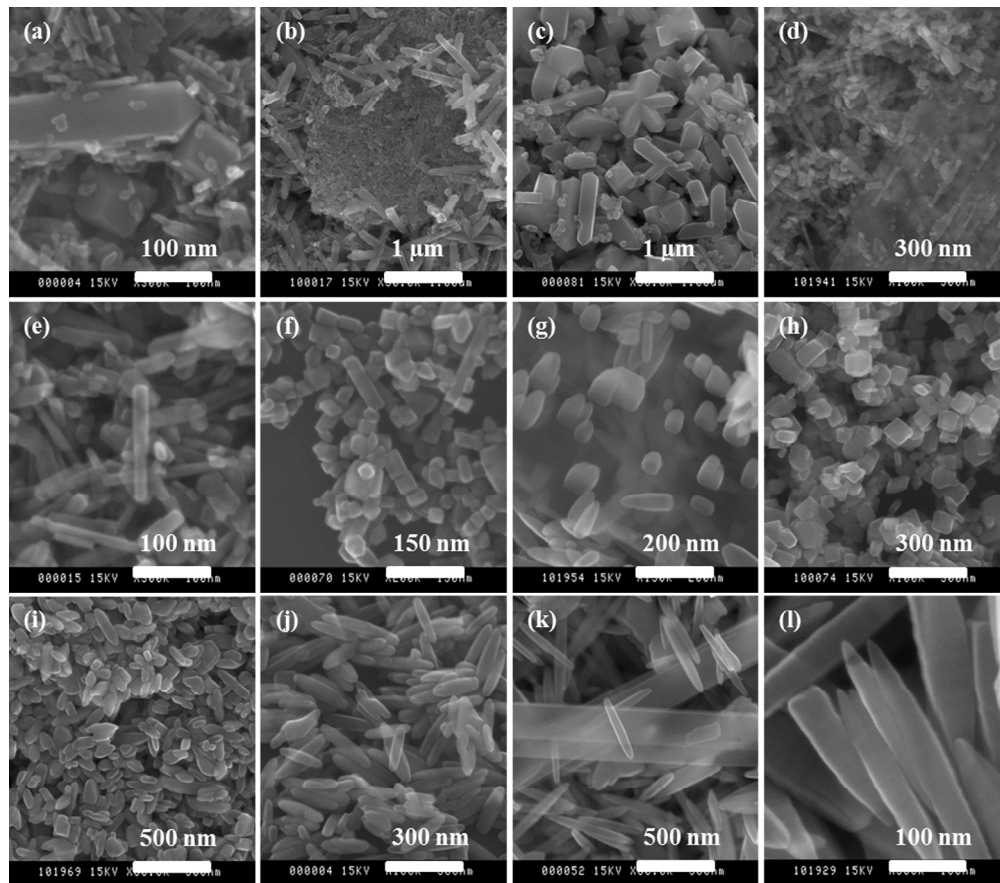
Fig. 4 FE-SEM images of (a) TMA-170-0.65, (b) TMA-170-0.56, (c) TMA-200-0.65, (d) TMA-140-3.2, (e) TMA-160-2.3, (f) TMA-200-3.6, (g) TMA-140-7.9, (h) TMA-170-7.3, (i) TMA-180-6.9, (j) TMA-200-6.7, (k) TMA-150-12, and (l) TMA-200-11.6 samples.
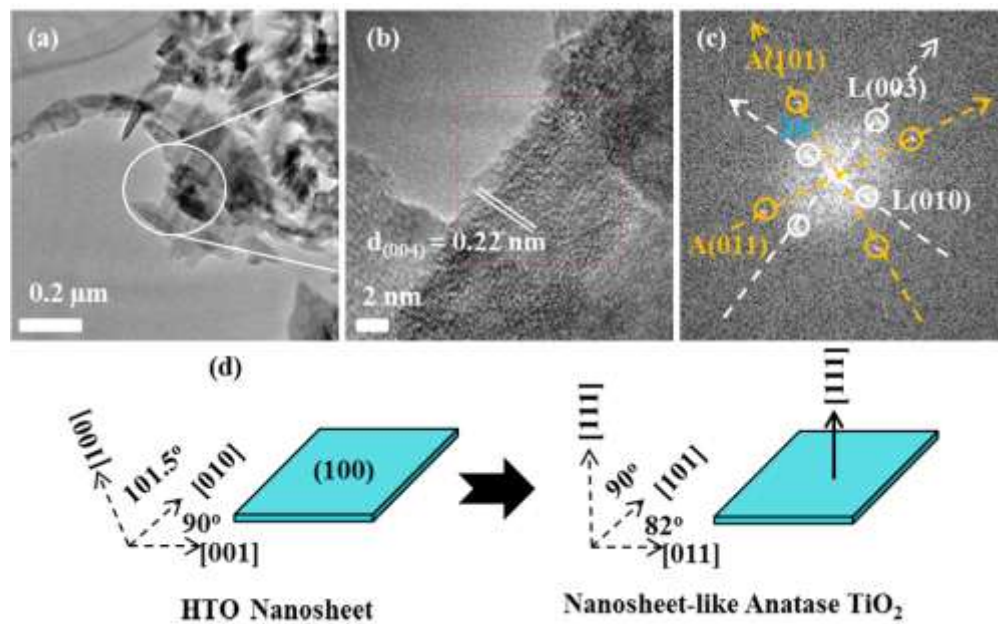171x150mm (300 x 300 DPI)

Fig. 5 TEM images and (c) FFT diffraction patterns of TMA-140-3.2 sample, and (d) structure transformation from layered structure to anatase structure.
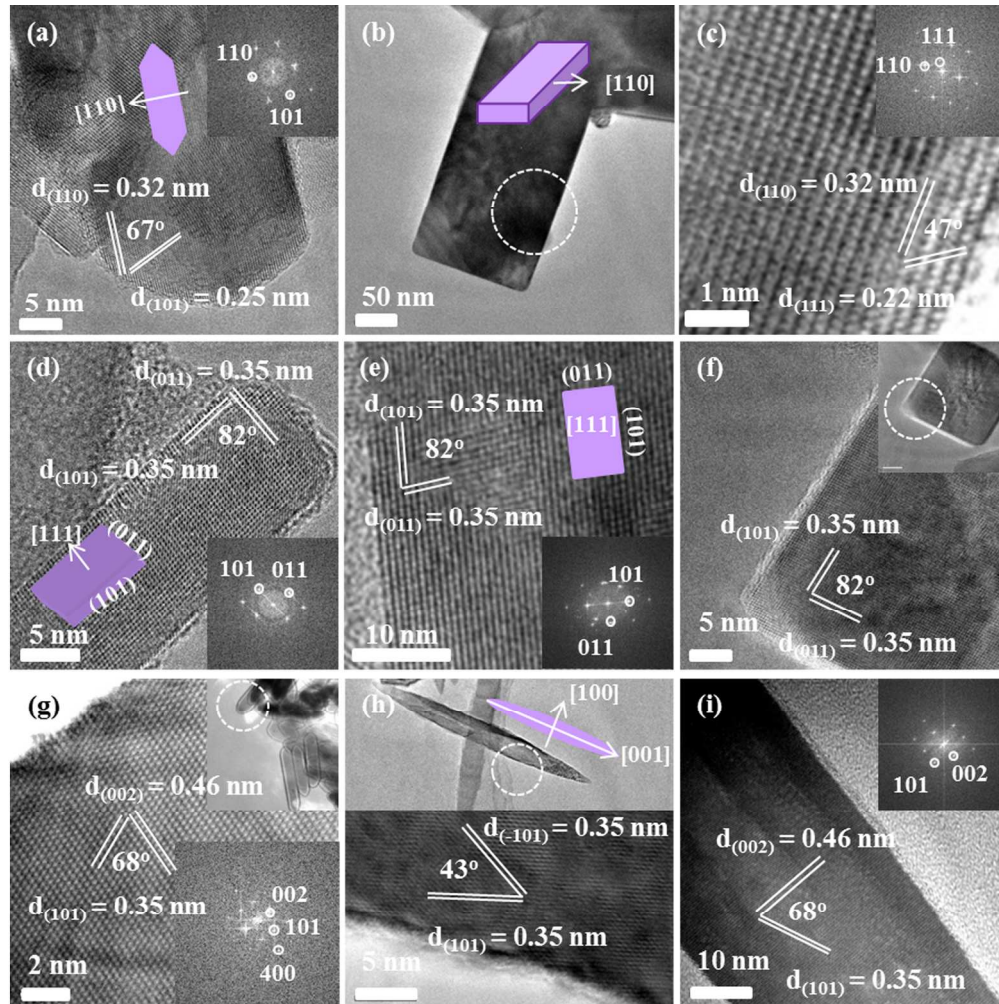82x52mm (300 x 300 DPI)

Fig. 6 TEM images and FFT diffraction patterns of (a) TMA-160-0.65, (b, c) TMA-200-0.65, (d) TMA-160-2.3, (e) TMA-200-3.6, (f) TMA-170-7.3, (g) TMA-200-6.7, (h) TMA-150-12, and (i) TMA-200-11.6 samples.
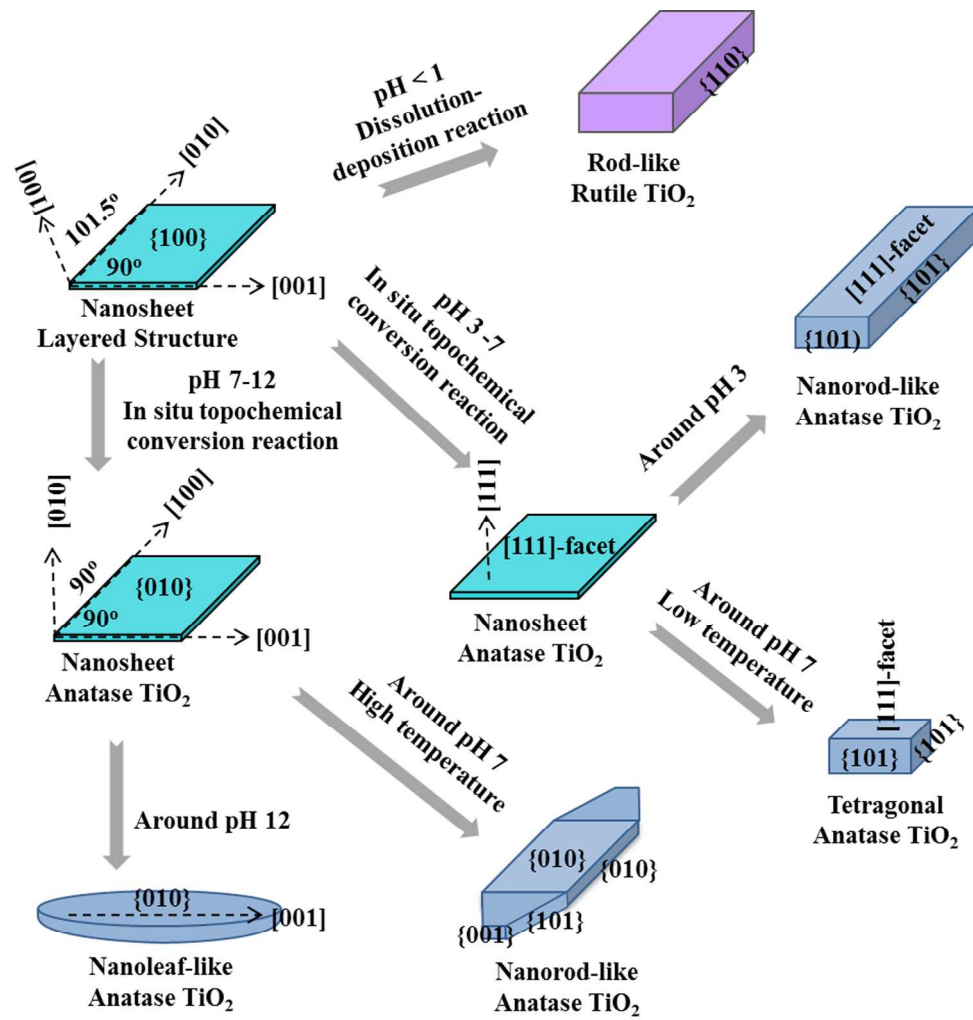171x171mm (300 x 300 DPI)

Fig. 7 Transformation reaction mechanism from TMA-HTO nanosheets to TiO2 nanocrystals.
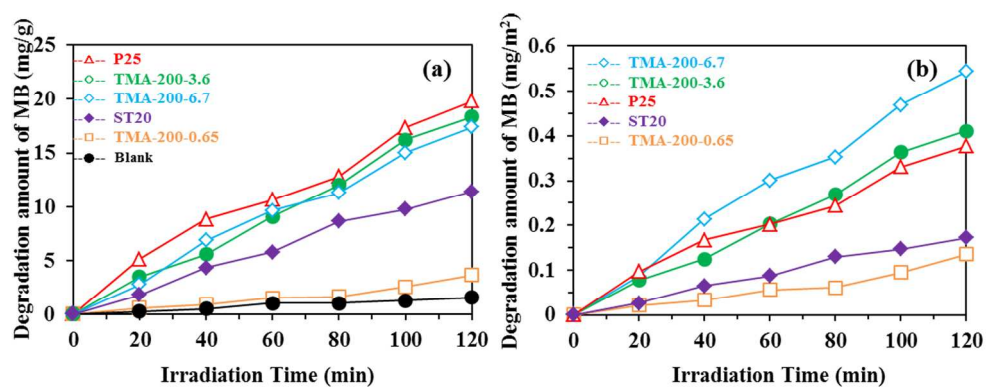171x174mm (300 x 300 DPI)

Fig. 8 Photocatalytic degradations of methylene blue (MB) by TMA-200-0.65 (rutile), TMA-200-3.6 ([111]-faceted anatase), TMA-200-6.7 ({010}-faceted anatase), P25 (partially [111]-faceted anatase), and ST20 (non-faceted anatase) samples presented by (a) mg(MB)/g(TiO2) and (b) mg(MB)/m2(TiO2), respectively. 171x70mm (300 x 300 DPI)
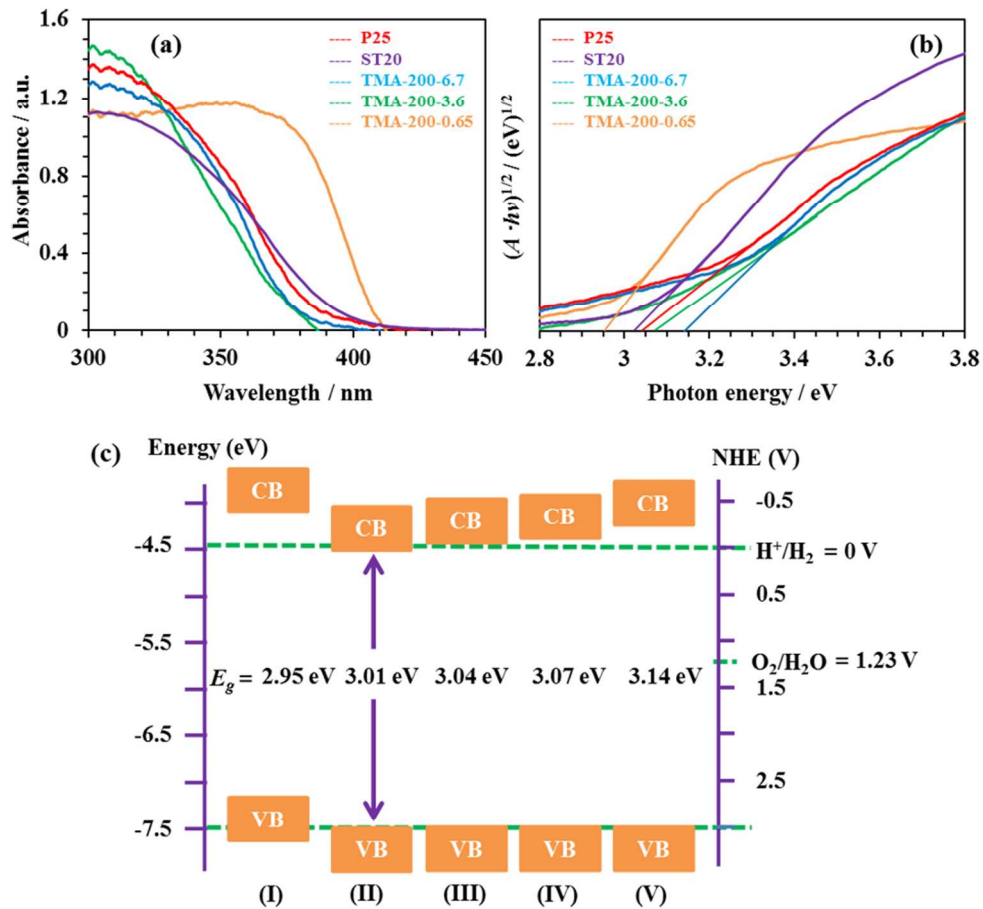
Fig. 9 (a) UV-visible absorption spectra; (b) the corresponding plots of transformed Kubelka-Munk function versus the energy of photon; (c) schematic illustration of the electronic band alignments of (I) TMA-200-0.65 (rutile), (II) ST20 (non-faceted anatase), (III) P25 (partially [111]-faceted anatase), (IV) TMA-200-3.6 ([111]-faceted anatase) and (V) TMA-200-6.7 ({010}-faceted anatase) samples.
82x76mm (300 x 300 DPI)